Chinese Journal of Aeronautics, (2014),27(4): 930–946

Chinese Society of Aeronautics and Astronautics
& Beihang University

Chinese Journal of Aeronautics

cja@buaa.edu.cn
www.sciencedirect.com

Dynamic modeling of a hose-drogue aerial refueling system and integral sliding mode backstepping control for the hose whipping phenomenon

Wang Haitao, Dong Xinmin *, Xue Jianping, Liu Jiaolong

Aeronautics and Astronautics Engineering College, Air Force Engineering University, Xi'an 710038, China

Received 24 July 2013; revised 26 October 2013; accepted 14 March 2014
Available online 5 July 2014

KEYWORDS

Aerial refueling;
Backstepping;
Hose drogue assembly;
Permanent magnet synchronous motor;
Sliding mode;
Whipping phenomenon

Abstract Dynamic modeling of a hose-drogue aerial refueling system (HDARS) and an integral sliding mode backstepping controller design for the hose whipping phenomenon (HWP) during probe-drogue coupling are studied. Firstly, a dynamic model of the variable-length hose-drogue assembly is built for the sake of exploiting suppression methods for the whipping phenomenon. Based on the lumped parameter method, the hose is modeled by a series of variable-length links connected with frictionless joints. A set of iterative equations of the hose's three-dimensional motion is derived subject to hose reeling in/out, tanker motion, gravity, and aerodynamic loads accounting for the effects of steady wind, atmospheric turbulence, and tanker wake. Secondly, relying on a permanent magnet synchronous motor and high-precision position sensors, a new active control strategy for the HWP on the basis of the relative position between the tanker and the receiver is proposed. Considering the strict-feedback configuration of the permanent magnet synchronous motor, a rotor position control law based on the backstepping method is designed to insure global stability. An integral of the rotor position error and an exponential sliding mode reaching law of the current errors are applied to enhance control accuracy and robustness. Finally, the simulation results show the effectiveness of the proposed model and control laws.

© 2014 Production and hosting by Elsevier Ltd. on behalf of CSAA & BUAA.
Open access under CC BY-NC-ND license.

1. Introduction

Autonomous aerial refueling (AAR) has received substantial attention from countries of the world spurred by a rapid integration of unmanned aerial vehicles (UAVs) into modern military missions.[1] Hose-drogue aerial refueling systems (HDARSs) are the most universal refueling equipment, and some outstanding progress has been made to automate the

* Corresponding author. Tel.: +86 29 84787400/801.
E-mail addresses: wanghaitao198638@163.com (H. Wang), dongxinmin@139.com (X. Dong), xiankgy@163.com (J. Xue), kgd_ljl@163.com (J. Liu).

Peer review under responsibility of Editorial Committee of CJA.

Production and hosting by Elsevier

http://dx.doi.org/10.1016/j.cja.2014.06.010
1000-9361 © 2014 Production and hosting by Elsevier Ltd. on behalf of CSAA & BUAA. Open access under CC BY-NC-ND license.

refueling process using vision-based control and navigation techniques recently.[2,3] Consequently, automation of hose-drogue-based refueling methods will have greater development potential in military and economic aspects.

It is also important to note that not all achievements of AAR are the result of improvement of UAV control and navigation, but the result of effective hose rewind control. As reported, if the reel is disabled during coupling, it is impossible for a receiver to couple without experiencing the so-called hose whipping phenomenon (HWP).[4] During coupling, the current pod is equipped with a tensator (spring-loaded take-up device)[5] to retract any slack in the hose as the probe pushes the drogue forward. If the tensator malfunctions or is subjected to an excessive closure speed during coupling, slack in the hose can form. When excessive slack occurs, the internal hose tension will rapidly decrease, and then the hose will violently whip due to aerodynamic forces. This phenomenon generates high loads on the hose and the probe, even damages them.[5] The HWP has been a serious constraint to AAR's success rates and security. Unfortunately, only a limited number of research on dynamic characteristics and control methods of the HWP can be found.

In order to further research dynamic characteristics of the HWP, many scholars and research institutions have conducted a lot of experiments and modeling analysis. NASA Dryden Flight Research Center[6,7] obtained abundant aerodynamic data specifically required in hose-drogue dynamic modeling by wind tunnel and flight tests. The Boeing Company[4,5] investigated dynamic characteristics of the KC-10 HWP by numerical simulation. Zhu and Meguid[8,9] proposed a new curved beam finite element formulation based on mechanics of materials to depict the dynamics of the hose-drogue assembly. Ro et al. tested the aerodynamic characteristics of the drogue by wind tunnel and computational fluid dynamics,[10] moreover gave a link-connected dynamic model of the hose-drogue assembly.[11,12] Although the models as mentioned above can reflect dynamics of the hose-drogue assembly, they cannot support exploiting HWP suppression methods due to the limitation of a constant hose length.

To keep the hose tension stable and suppress the HWP, every pod is equipped with a tensator at present. However, a hose-drogue system suffered a 2.5% failure rate when the hose slackened and lost the stability.[8] The Boeing Company[4] confirmed that the reel take-up speed lagging behind the closure speed was responsible for the failure by numerical simulation. Ro et al.[13] tried to improve the control law of the tensator ignoring the difficulty of mechanism rebuilding. Recently, the integration of a permanent magnet synchronous motor (PMSM) and high-precision position sensors into the refueling pod provides another chance for high-performance suppression methods for the HWP. Alden and Vennero[14] invented a new refueling pod with a reel driven by a PMSM. Liu and Sun[15] achieved position tracking for nominal model-based through sliding mode control with backstepping. Yang et al.[16] proposed an integral sliding mode backstepping speed control for high-altitude electric propulsion systems. Zhang et al.[17] designed a PMSM nonlinear speed control method using sliding-mode control and disturbance compensation techniques. Bartov[18] achieved relative position communion by three position sensors installed in the tanker, receiver, and drogue, respectively.

In this paper, a link-connected dynamic model of the hose-drogue assembly with a variable length is built. Then reeling in/out of the hose is converted into a PMSM's rotor angular position control, and a nonlinear controller based on backstepping with integral and sliding mode action for the HWP is derived. Finally, characteristics of the HWP are analyzed, while the model and the controller are validated by numerical simulation.

2. Dynamic modeling of an HDARS

2.1. Equation of motion of the hose-drogue assembly

2.1.1. Modeling assumptions and definition of coordinate systems

The reel, hose, and drogue are the key parts of an HDARS for suppressing the HWP, transferring fuel, and assisting hookup. The PMSM drives the reel to deploy and retrieve the hose through a reducer.

Based on the lumped parameter method, the variable-length hose-drogue assembly is discretized as a link-connected system, where the hose consists of a finite number of variable-length links connected with frictionless joints. The masses and forces associated with each link are concentrated at the joints. The drogue is treated as a mass point at the end of the hose.[11,12] The twist around the hose central axis and the property of elasticity and damping of the hose are neglected here. The configuration, modeling assumptions, and definition of coordinates of the HDARS are illustrated in Fig. 1.

As shown in Fig. 1, $O_gX_gY_gZ_g$ represents an inertial reference coordinate system. The equation of motion of the hose-drogue assembly is deduced in the towing point coordinate system $O_WX_WY_WZ_W$. The axes of $O_WX_WY_WZ_W$ are parallel to the trajectory coordinate of the tanker $O_TX_TY_TZ_T$. The orientations of the Kth link are described relative to $O_WX_WY_WZ_W$ using the angles θ_{K1} and θ_{K2} respectively relative to the planes $O_WX_WY_W$ and $O_WX_WZ_W$.

2.1.2. Kinematics analysis

As shown in Fig. 1, the position vector $\boldsymbol{r}_K$ of joint K relative to $O_WX_WY_WZ_W$ is expressed as

$$\boldsymbol{r}_K = \boldsymbol{r}_{K-1} + \boldsymbol{p}_K \tag{1}$$

where $\boldsymbol{p}_K$ is the position vector from joint $K-1$ to joint K. The coordinates of $\boldsymbol{p}_K$ in $O_WX_WY_WZ_W$ can be written as

$$\boldsymbol{p}_K = -l_K[\,C_1C_2 \quad S_2 \quad -S_1C_2\,]^{\mathrm{T}} \tag{2}$$

where $C_i = \cos\theta_{Ki}$ and $S_i = \sin\theta_{Ki}$ $(i = 1, 2)$; l_K is the length of the Kth link. To describe the hose reeling in/out, l_K is regarded as a variable.

The velocity $\boldsymbol{v}_K$ and acceleration $\boldsymbol{a}_K$ of the Kth joint can be found by differentiating Eq. (1):

$$\begin{cases} \boldsymbol{v}_K = \boldsymbol{v}_{K-1} + \dot{\boldsymbol{p}}_K \\ \boldsymbol{a}_K = \boldsymbol{a}_{K-1} + \ddot{\boldsymbol{p}}_K \end{cases} \tag{3}$$

Considering the transport motion as the plane motion of $O_WX_WY_WZ_W$ relative to $O_gX_gY_gZ_g$, namely the attitude variation of the tanker, the first and second derivatives of $\boldsymbol{p}_K$ by differentiating Eq. (3) can be expressed as

$$\dot{\boldsymbol{p}}_K = \sum_{i=1}^{2}(\boldsymbol{p}_{K,\theta_{Ki}}\dot{\theta}_{Ki}) + \boldsymbol{p}_{K,l_K}\dot{l}_K + (\boldsymbol{\omega}_W \times \boldsymbol{p}_K) \tag{4}$$

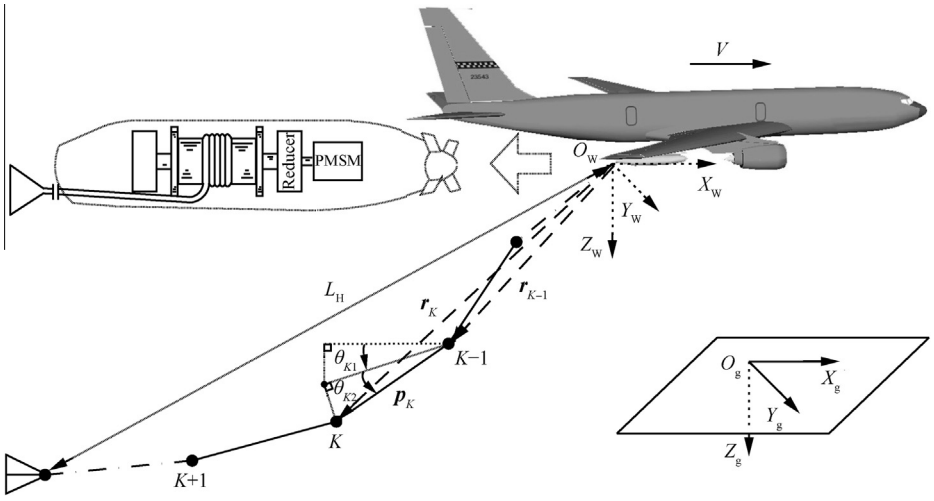

Fig. 1 Configuration, modeling assumptions, and definition of coordinate systems.

$$\ddot{\boldsymbol{p}}_K = \sum_{i=1}^{2}(\boldsymbol{p}_{K,\theta_{Ki}}\ddot{\theta}_{Ki} + \dot{\boldsymbol{p}}_{K,\theta_{Ki}}\dot{\theta}_{Ki}) + \boldsymbol{p}_{K,l_K}\ddot{l}_K + \dot{\boldsymbol{p}}_{K,l_K}\dot{l}_K + (\boldsymbol{\alpha}_W \times \boldsymbol{p}_K) + (\boldsymbol{\omega}_W \times \dot{\boldsymbol{p}}_K) \tag{5}$$

where $\boldsymbol{p}_{K,\theta_{Ki}} = \partial \boldsymbol{p}_K/\partial\theta_{Ki}$ and $\boldsymbol{p}_{K,l_K} = \partial \boldsymbol{p}_K/\partial l_K$. $\boldsymbol{\omega}_W$, $\boldsymbol{\alpha}_W$, $\boldsymbol{\omega}_W \times \boldsymbol{p}_K$, $\boldsymbol{\alpha}_W \times \boldsymbol{p}_K$, and $\boldsymbol{\omega}_W \times \dot{\boldsymbol{p}}_K$ represent the angular velocity, angular acceleration, velocity, acceleration, and Coriolis acceleration of $O_W X_W Y_W Z_W$'s transport motion relative to $O_g X_g Y_g Z_g$. Because the mass of each link is low and varies slowly, complementary acceleration resulting from mass variation of the hose is neglected in Eq. (5).

Noting $\boldsymbol{p}_{K,\theta_{K1}} \cdot \boldsymbol{p}_{K,\theta_{K2}} = 0$ and taking the scalar product of Eq. (5) with $\boldsymbol{p}_{K,\theta_{Ki}}$, the second-order derivative of the angles for any link can be written as

$$\ddot{\theta}_{Ki} = \boldsymbol{p}_{K,\theta_{Ki}} \cdot \left[\boldsymbol{a}_K - \boldsymbol{a}_{K-1} - \sum_{j=1}^{2}(\dot{\boldsymbol{p}}_{K,\theta_{Kj}}\dot{\theta}_{Kj}) - \boldsymbol{p}_{K,l_K}\ddot{l}_K - \dot{\boldsymbol{p}}_{K,l_K}\dot{l}_K - (\boldsymbol{\alpha}_W \times \boldsymbol{p}_K) - (\boldsymbol{\omega}_W \times \dot{\boldsymbol{p}}_K)\right] \Big/ (\boldsymbol{p}_{K,\theta_{Ki}} \cdot \boldsymbol{p}_{K,\theta_{Ki}}) \tag{6}$$

Since $\boldsymbol{p}_{K,\theta_{K1}} \cdot \boldsymbol{p}_{K,\theta_{K1}} = l_K^2 C_2^2$ and $\boldsymbol{p}_{K,\theta_{K2}} \cdot \boldsymbol{p}_{K,\theta_{K2}} = l_K^2$, the denominator in Eq. (6) will be 0 from a mathematical perspective, when $\theta_{K2} = \pm\pi/2$ or $l_K = 0$. However, θ_{K2} never reaches $\pm\pi/2$ in a normal refueling flight due to the aerodynamic damping effect and l_K can be avoided to approach 0 artificially in modeling. Therefore, the denominator in Eq. (6) will not be 0 in modeling. Eq. (6) is the equation of motion of the Kth link, which can be used recursively to describe the motions of all links under a prescribed attitude variation of the tanker.

2.1.3. Dynamic analysis

According to Newton's second law, the acceleration $\boldsymbol{a}_K$ of joint K is expressed as

$$\boldsymbol{a}_K = (\boldsymbol{Q}_K + \boldsymbol{t}_K - \boldsymbol{t}_{K+1})/m_K \tag{7}$$

where m_K is the mass of the Kth link and $m_K = l_K\mu$, in which μ is the mass per unit length; $\boldsymbol{t}_K$ is the tension vector of the Kth link; $\boldsymbol{Q}_K$ is the resultant force vector acting on joint K, which includes gravity and aerodynamic loads accounting for the effects of steady wind, tanker wake, and atmospheric turbulence.

$\boldsymbol{t}_K$ is an internal force and cannot be obtained directly. According to the definition, $\boldsymbol{p}_K$ meets the following geometrical constraints:

$$\boldsymbol{p}_K \cdot \boldsymbol{p}_K = l_K^2 \tag{8}$$

Considering that all the links have variable lengths, differentiate Eq. (8) twice to get the equation as follows:

$$\dot{\boldsymbol{p}}_K \cdot \dot{\boldsymbol{p}}_K + \boldsymbol{p}_K \cdot \ddot{\boldsymbol{p}}_K = \dot{l}_K^2 + l_K\ddot{l}_K \tag{9}$$

Substituting $\boldsymbol{p}_K = -l_K\boldsymbol{n}_K$, $\dot{\boldsymbol{p}}_K = -\dot{l}_K\boldsymbol{n}_K - l_K\dot{\boldsymbol{n}}_K$, and Eq. (3) into Eq. (9) gives the accelerations of adjacent joints as follows:

$$(\boldsymbol{a}_K - \boldsymbol{a}_{K-1}) \cdot \boldsymbol{n}_K = l_K\dot{\boldsymbol{n}}_K \cdot \dot{\boldsymbol{n}}_K - \ddot{l}_K \tag{10}$$

where $\boldsymbol{n}_K = [\,C_1C_2 \quad S_2 \quad -S_1C_2\,]^T$.

Substituting Eq. (7) into Eq. (10) gives a set of linear algebraic equations for the link tensions

$$\frac{\boldsymbol{n}_K \cdot \boldsymbol{n}_{K-1}}{m_{K-1}}t_{K-1} - \left(\frac{1}{m_{K-1}} + \frac{1}{m_K}\right)t_K + \frac{\boldsymbol{n}_K \cdot \boldsymbol{n}_{K+1}}{m_K}t_{K+1} = \ddot{l}_K - l_K\dot{\boldsymbol{n}}_K \cdot \dot{\boldsymbol{n}}_K - \left(\frac{\boldsymbol{Q}_{K-1}}{m_{K-1}} - \frac{\boldsymbol{Q}_K}{m_K}\right) \cdot \boldsymbol{n}_K \tag{11}$$

where $t_K = \|\boldsymbol{t}_K\|$.

If the hose consists of N links and all the links have a uniform length, namely $l_1 = l_2 = \cdots = l_N = l_c$ and $m_1 = m_2 = \cdots = m_N = m_c$, Eq. (11) can be simplified as

$$(\boldsymbol{n}_K \cdot \boldsymbol{n}_{K-1})t_{K-1} - 2t_K + (\boldsymbol{n}_K \cdot \boldsymbol{n}_{K+1})t_{K+1} = m_c(\ddot{l}_c - l_c\dot{\boldsymbol{n}}_K \cdot \dot{\boldsymbol{n}}_K) - (\boldsymbol{Q}_{K-1} - \boldsymbol{Q}_K) \cdot \boldsymbol{n}_K \tag{12}$$

Eq. (12) is recursively written in the matrix form $\boldsymbol{A}\cdot\boldsymbol{t} = \boldsymbol{q}$ as follows:

$$\begin{bmatrix} -1 & \boldsymbol{n}_1 \cdot \boldsymbol{n}_2 & 0 & \cdots & 0 \\ \boldsymbol{n}_2 \cdot \boldsymbol{n}_1 & -2 & \boldsymbol{n}_2 \cdot \boldsymbol{n}_3 & \ddots & \vdots \\ 0 & \ddots & \ddots & \ddots & 0 \\ \vdots & \ddots & \boldsymbol{n}_{N-1} \cdot \boldsymbol{n}_{N-2} & -2 & \boldsymbol{n}_{N-1} \cdot \boldsymbol{n}_N \\ 0 & \cdots & 0 & \boldsymbol{n}_N \cdot \boldsymbol{n}_{N-1} & -2 \end{bmatrix} \begin{bmatrix} t_1 \\ t_2 \\ t_3 \\ \vdots \\ t_N \end{bmatrix} = \begin{bmatrix} m_c(\ddot{l}_c - l_c\dot{\boldsymbol{n}}_1 \cdot \dot{\boldsymbol{n}}_1) - (\boldsymbol{a}_0 m_c - \boldsymbol{Q}_1) \cdot \boldsymbol{n}_1 \\ m_c(\ddot{l}_c - l_c\dot{\boldsymbol{n}}_2 \cdot \dot{\boldsymbol{n}}_2) - (\boldsymbol{Q}_1 - \boldsymbol{Q}_2) \cdot \boldsymbol{n}_2 \\ \vdots \\ m_c(\ddot{l}_c - l_c\dot{\boldsymbol{n}}_N \cdot \dot{\boldsymbol{n}}_N) - (\boldsymbol{Q}_{N-1} - \boldsymbol{Q}_N) \cdot \boldsymbol{n}_N \end{bmatrix} \tag{13}$$

where $\boldsymbol{a}_0$ is the acceleration of the refueling pod relative to $O_gX_gY_gZ_g$. The impact of the tanker motion on the dynamics of the hose is fully reflected through $\boldsymbol{a}_0$, $\boldsymbol{\alpha}_W$, and $\boldsymbol{\omega}_W$ in Eq. (6). Evidently, Eq. (13) always has a unique solution $\boldsymbol{t} = \boldsymbol{A}^{-1}\boldsymbol{q}$.

2.1.4. External forces analysis

The resultant external force $\boldsymbol{Q}_K$ acting on joint K including the gravity $m_K\boldsymbol{g}$ and the aerodynamic forces $\boldsymbol{D}_K$ can be written as

$$\boldsymbol{Q}_K = m_K\boldsymbol{g} + (\boldsymbol{D}_{K-1} + \boldsymbol{D}_K)/2 \tag{14}$$

where $\boldsymbol{D}_K$ can be computed as[4]

$$\begin{aligned}\boldsymbol{D}_K = &\left[-\frac{1}{2}\rho(\boldsymbol{V}_{K/\text{air}}\cdot\boldsymbol{n}_K)^2\pi d_K l_K c_{t,K}\right]\boldsymbol{n}_K \\ &+\left[-\frac{1}{2}\rho\|\boldsymbol{V}_{K/\text{air}} - (\boldsymbol{V}_{K/\text{air}}\cdot\boldsymbol{n}_K)\boldsymbol{n}_K\|d_K l_K c_{\text{n},K}\right] \\ &\times\left[\boldsymbol{V}_{K/\text{air}} - (\boldsymbol{V}_{K/\text{air}}\cdot\boldsymbol{n}_K)\boldsymbol{n}_K\right]\end{aligned} \tag{15}$$

where $\boldsymbol{V}_{K/\text{air}} = \boldsymbol{v}_K - \boldsymbol{u}_K$, in which $\boldsymbol{u}_K$ is the local air velocity including steady wind, tanker wake, and turbulence at joint K; ρ_∞ is the air density. d_K is the diameter of the hose; $c_{t,K}$ is the skin friction coefficient. $c_{\text{n},K}$ is the drag coefficient.

The resultant external force $\boldsymbol{Q}_N$ of the drogue can be written as[11,12]

$$\boldsymbol{Q}_N = (m_N + m_{\text{drogue}})\boldsymbol{g} + \boldsymbol{D}_N/2 + \boldsymbol{D}_{\text{drogue}} \tag{16}$$

where m_{drogue} is the mass of the drogue. $\boldsymbol{D}_N$ is the drag of the Nth link. The drag of the drogue $\boldsymbol{D}_{\text{drogue}}$ can be computed as

$$\boldsymbol{D}_{\text{drogue}} = -\frac{1}{2}\rho_\infty\|\boldsymbol{V}_{N/\text{air}}\|\left(\frac{\pi d_{\text{drogue}}^2}{4}\right)c_{\text{drogue}}\boldsymbol{V}_{N/\text{air}} \tag{17}$$

where d_{drogue} is the diameter of the drogue and c_{drogue} is the drag coefficient.

2.2. Modeling of PMSM, reducer, and reel

Assuming the reel is driven by the PMSM through a reducer to reel in/out of the hose and there are no magnetic saturation, hysteresis, eddy current loss, and friction of the reducer, excluding sinusoidal magnetic field distribution, the mathematical model of the PMSM can be described in the $d-q$ coordinate system as follows:[16]

$$\begin{cases}\dfrac{\mathrm{d}\vartheta}{\mathrm{d}t} = \omega \\ \dfrac{\mathrm{d}\omega}{\mathrm{d}t} = \dfrac{3P\psi_f}{2J}i_q - \dfrac{B}{J}\omega - \dfrac{T_L}{J} \\ \dfrac{\mathrm{d}i_q}{\mathrm{d}t} = -\dfrac{R}{L_s}i_q - P\omega i_d - \dfrac{P\psi_f}{L_s}\omega + \dfrac{1}{L_s}u_q \\ \dfrac{\mathrm{d}i_d}{\mathrm{d}t} = -\dfrac{R}{L_s}i_d + P\omega i_q + \dfrac{1}{L_s}u_d\end{cases} \tag{18}$$

where ω is the rotor angular velocity, ϑ is the rotor angular position, R is the stator resistance, L_s is the stator inductance, P is the number of pole pairs, ψ_f is the stator flux linkage, J is the moment of inertia, B is the viscous friction coefficient, and T_L is the load torque. i_d, i_q, u_d, and u_q are d, q axis currents and voltages, respectively.

According to the kinematics, the length L, speed $\dot{L}$, acceleration $\ddot{L}$ of the hose can be expressed as functions of the PMSM's rotor angular position ϑ as follows:

$$\begin{cases}L = \vartheta r/i \\ \dot{L} = \dot{\vartheta} r/i \\ \ddot{L} = \ddot{\vartheta} r/i\end{cases} \tag{19}$$

where r is the radius of the reel and i is the reduction ratio of the reducer.

Length control of the hose can be converted into rotor angular position control of the PMSM through Eq. (19). Then keeping the hose tension stable and suppressing the HWP can be achieved by the PMSM.

3. HWP suppression based on PMSM integral sliding mode backstepping position control

3.1. Limitations of tensator for HWP

The hose tension $\boldsymbol{T}_{\text{reel}}$ generated by the reel driven by the tensator can be formulated as[4]

$$\boldsymbol{T}_{\text{reel}} = \boldsymbol{T}_{\text{static}}[1 - (L_0 - L)/L_1] \tag{20}$$

where $\boldsymbol{T}_{\text{static}}$ is the hose tension at the exit of the pod before coupling; L_0, L, and L_1 are the initial length, the full hose length, and the controllable hose length by the tensator, respectively.

The acceleration of the hose reeling in/out can be expressed as

$$\ddot{L} = (\boldsymbol{T}_{\text{reel}} - \boldsymbol{T}_{\text{hose}})/M \tag{21}$$

where $\boldsymbol{T}_{\text{hose}}$ is the hose tension at the exit of the pod and $\boldsymbol{T}_{\text{hose}} = \boldsymbol{t}_1$; M is the mass of the reel plus any hose that has been wrapped around the reel.

From Eqs. (20), (21), the tensator is a passive control for the HWP based on the spring. Once excessive slack occurs, the redundant length of the hose can exceed the control range due to the limited value of L_1, and the tensator will lose its desired function. The speed of hose reeling in/out cannot match the closure speed of the receiver. Because $\ddot{L}$ becomes lower as the hose is reeled in, the time-lag effect of control will be more obvious.

3.2. PMSM integral sliding mode backstepping position control for HWP

The most effective way to suppress the HWP is to stabilize the hose tension by real-time active hose reeling in/out on the basis of the relative position between the tanker and the receiver. Through Eq. (19), hose reeling in/out can be converted to PMSM rotor angular position control.

Considering the strict-feedback structure[19] of the PMSM, the backstepping approach is adopted to ensure global stability. In the process of backstepping, an integral factor of the rotor angular position error is applied to improve position tracking precision; the exponential reaching law is used to construct the sliding mode surface equations of the d/q axis current error to ensure convergence speed and robustness.

The proposed control system is designed to achieve the angular position-tracking objective as follows:

$$\lim_{t\to\infty}(\vartheta - \vartheta^*) = 0 \tag{22}$$

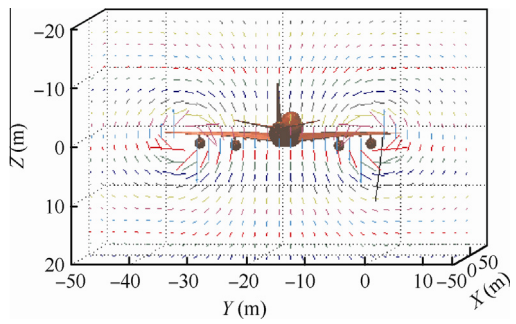

Fig. 2 Vertical slice of tanker wake 10 m behind tanker.

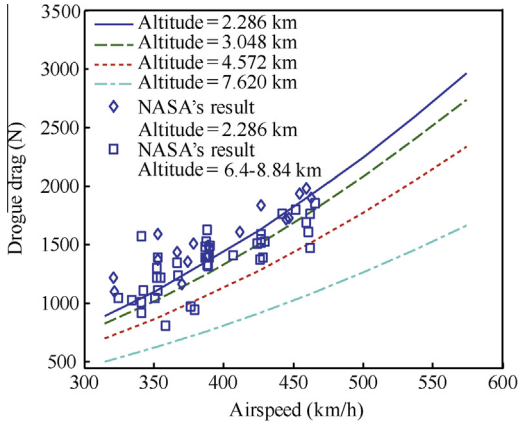

Fig. 3 Steady-state drogue drag and flight-test data from NASA.[6]

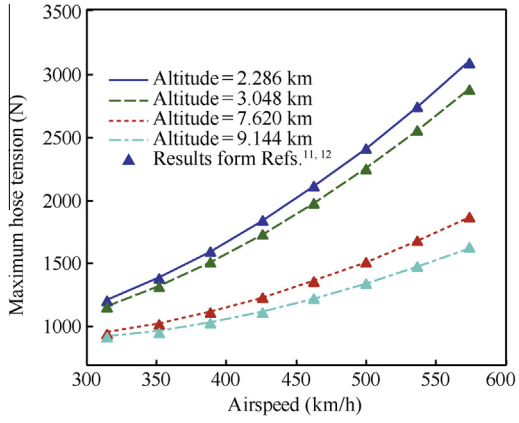

Fig. 4 Steady-state maximum hose tension and research results from Refs.[11,12]

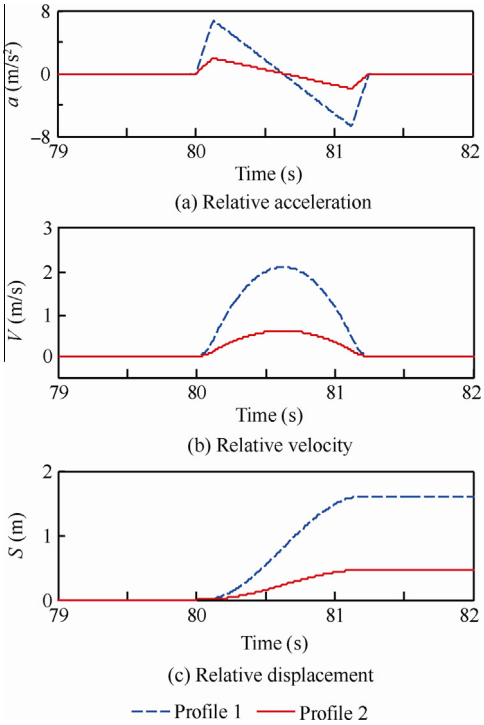

Fig. 5 Two types of relative coupling profile.

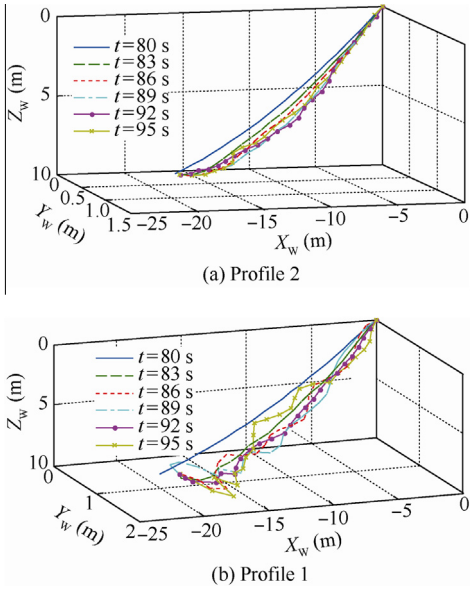

Fig. 6 Hose geometry (22.86 m) history along two types of relative coupling profile.

where ϑ^* is the reference angular position.

To maximize the output torque, the space vector modulation (SVM) method is commonly used for a PMSM. The simplest and most efficient way in the SVM is[15]

$$i_d^* = 0 \tag{23}$$

where i_d^* is the reference d axis current.

Under this condition, the electric torque of the PMSM can be expressed as[17]

$$T_e = 3p\psi_f i_q/2 \tag{24}$$

Define tracking errors of each subsystem of the PMSM as follows:

$$\begin{cases} e_1 = \vartheta - \vartheta^* \\ e_2 = \omega - \omega^* \\ e_3 = i_q - i_q^* \\ e_4 = i_d - i_d^* \end{cases} \tag{25}$$

where ϑ^*, ω^*, i_q^*, and i_d^* are the corresponding reference commands for each subsystem.

The proposed control system is designed step by step as follows.

Step 1 For the subsystem of e_1, the Lyapunov function about e_1 is chosen as

$$V_1 = \frac{1}{2}kz_1^2 + \frac{1}{2}e_1^2 \tag{26}$$

where $k > 0$, and z_1 is the integral of e_1, i.e.

$$z_1 = \int_0^t e_1(t)\mathrm{d}t \tag{27}$$

By integrating this integral action into the Lyapunov function, the convergence of e_1 to zero can be ensured despite the presence of the disturbance.

The derivative of Eq. (26) is

$$\dot{V}_1 = kz_1e_1 + e_1(\omega - \dot{\vartheta}^*) \tag{28}$$

To keep Eq. (28) nonpositive definite, the virtual control command of ω is chosen as

$$\omega^* = \dot{\vartheta}^* - kz_1 - k_1e_1 \tag{29}$$

where $k_1 > 0$.

Using Eqs. (28) and (29), the derivative of V_1 can be derived as

$$\dot{V}_1 = -k_1e_1^2 \leqslant 0 \tag{30}$$

Step 2 For the subsystem of e_2, the Lyapunov function of e_2 is chosen as

$$V_2 = V_1 + \frac{1}{2}e_2^2 \tag{31}$$

The derivative of e_2 is

$$\dot{e}_2 = \frac{3P\psi_f}{2J}i_q + \left(k_1 - \frac{B}{J}\right)\omega - \frac{T_L}{J} + ke_1 - k_1\dot{\vartheta}^* - \ddot{\vartheta}^* \tag{32}$$

Substituting Eqs. (30) and (32) into Eq. (31), the derivative of V_2 can be derived as

$$\dot{V}_2 = -k_1e_1^2 + e_2\left[\frac{3P\psi_f}{2J}i_q + \left(k_1 - \frac{B}{J}\right)\omega - \frac{T_L}{J} + ke_1 - k_1\dot{\vartheta}^* - \ddot{\vartheta}^*\right] \tag{33}$$

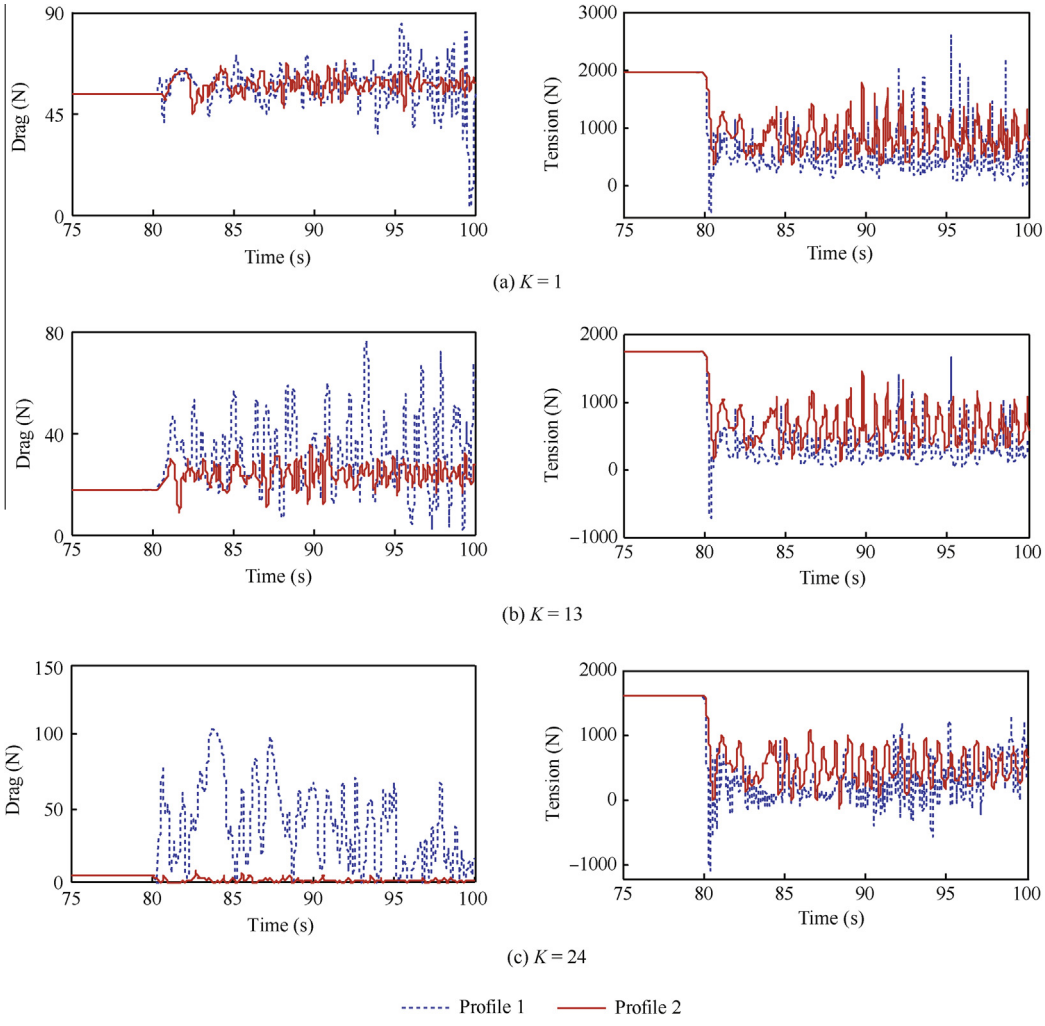

Fig. 7 Drags and tensions of hose along two types of relative coupling profile.

To keep Eq. (33) nonpositive definite, the virtual control command of i_q is chosen as

$$i_q^* = -\frac{2}{3P\psi_f}\left[(k_1 J - B)\omega + kJe_1 + k_2 Je_2 - k_1 J\dot{\vartheta}^* - J\ddot{\vartheta}^* - T_L\right] \tag{34}$$

where $k_2 > 0$.

Using Eqs. (33) and (34) gives

$$\dot{V}_2 = -k_1 e_1^2 - k_2 e_2^2 \leqslant 0 \tag{35}$$

Considering mechanical inertia, the transfer function from the hose tension to T_L in Eq. (34) can be written as

$$T_L = \frac{r}{i}\cdot\frac{1}{s+1}t_1 \tag{36}$$

Step 3 The stator currents response much more quickly than the rotor angular velocity ω. To ensure convergence speed and robustness with disturbance resulted from the load torque T_L and parameters, the exponential reaching law is used to construct the sliding mode surface equation of the q axis current error:

$$\dot{s}_1 = -a_1 s_1 - \rho_1 \mathrm{sgn}(s_1) \tag{37}$$

where $s_1 = c_1 e_3$, $c_1 > 0$, $a_1 > 0$, $\rho_1 > 0$, and sgn(*) is a symbolic function.

Using Eqs. (18), (25), (34), and (37), the real q axis voltage input is expressed as

$$\begin{aligned} u_q = {} & Ri_q + PL_s\omega i_d + P\psi_f\omega + L_s\left\{\frac{-a_1 s_1 - \rho_1\mathrm{sgn}(s_1)}{c_1}\right. \\ & -\frac{2J}{3P\psi_f}\left[\left(k_1 + k_2 - \frac{B}{J}\right)\frac{3P\psi_f}{2J}i_q + \left(\frac{B^2}{J^2} - k_1\frac{B}{J}\right.\right. \\ & \left.\left.-k_2\frac{B}{J} + k_1 k_2 + k\right)\omega + kk_2 e_1 - (k + k_1 k_2)\dot{\vartheta}^* \right. \\ & \left.\left.-(k_1 + k_2)\ddot{\vartheta}^* - \dddot{\vartheta}^* - \left(k_1 + k_2 - \frac{B}{J}\right)\frac{T_L}{J} - \frac{\dot{T}_L}{J}\right]\right\} \end{aligned} \tag{38}$$

Similarly, the sliding mode surface equation of the d axis current error is designed using the exponential reaching law as

$$\dot{s}_2 = -a_2 s_2 - \rho_2 \mathrm{sgn}(s_2) \tag{39}$$

where $s_2 = c_2 e_4$, $c_2 > 0$, $a_2 > 0$, and $\rho_2 > 0$.

Using Eqs. (18), (23), (25), and (39), the real d axis voltage input is expressed as

$$u_d = Ri_d - PL_s\omega i_q + L_s[-a_2 s_2 - \rho_2\mathrm{sgn}(s_2)]/c_2 \tag{40}$$

The reference angular position command ϑ^* can be transformed into the relative position between the probe and the pod by Eq. (19) as

$$\vartheta^* = iL/r \tag{41}$$

where L is a function of the relative distance between the probe and the pod, and

$$L = \eta\sqrt{\Delta x^2 + \Delta y^2 + \Delta z^2} - L_0 \tag{42}$$

where $\eta = L_0/L_H$ (L_H, see Fig. 1), which reflects the degree of hose slack. Δx, Δy, and Δz are three spatial components of the relative distance between the probe and the pod, respectively, which can be accurately measured by three position sensors respectively installed on the tanker, receiver, and drogue.[18]

Consequently, $\dot{\vartheta}^*$, $\ddot{\vartheta}^*$, and $\dddot{\vartheta}^*$ in Eqs. (34) and (38) can be derived by differentiating the relative distance between the probe and the pod through Eqs. (41), (42). Through this conversion, ϑ^*, $\dot{\vartheta}^*$, $\ddot{\vartheta}^*$, and $\dddot{\vartheta}^*$ can satisfy continuous, bounded, and available[19] online. The control laws can completely match the coupling profile by the receiver, because ϑ^*, $\dot{\vartheta}^*$, $\ddot{\vartheta}^*$, and $\dddot{\vartheta}^*$ imply all the information about the coupling profile.

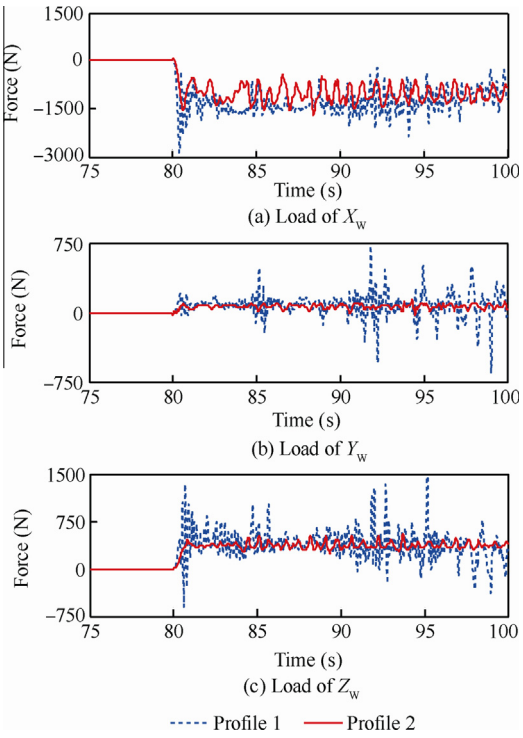

Fig. 8 External forces on probe along two types of relative coupling profile.

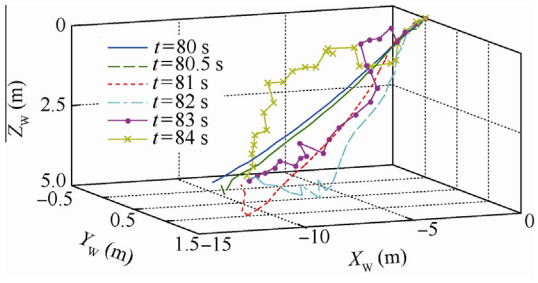

Fig. 9 Hose geometry (14.33 m) history adopting coupling Profile 1.

To eliminate the chattering phenomenon of sliding mode control, the symbolic function is substituted by the nonlinear function as follows:[20]

$$s_i/(|s_i| + \sigma_i) \tag{43}$$

where σ_i is a little positive constant.

3.3. Global stability of control system

Using the control laws of Eqs. (38) and (40), the global asymptotical stability can be guaranteed for the PMSM like Eq. (18).

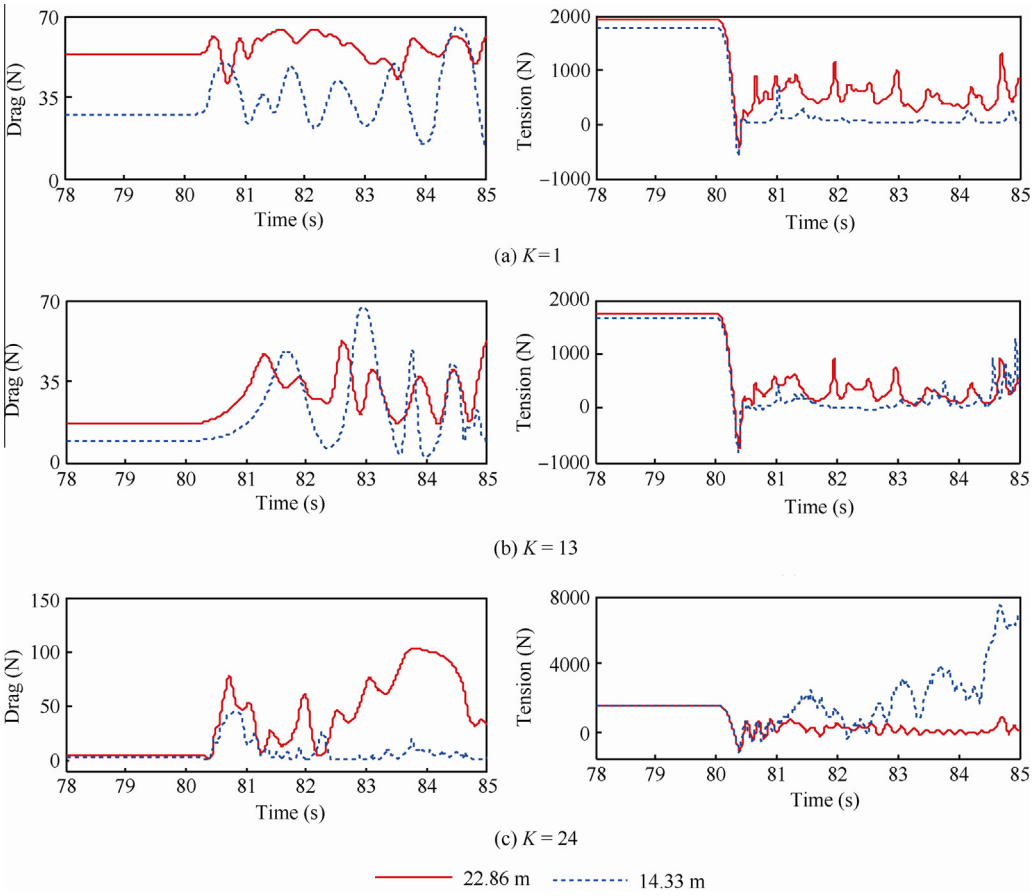

Fig. 10 Drags and tensions of hose adopting coupling Profile 1.

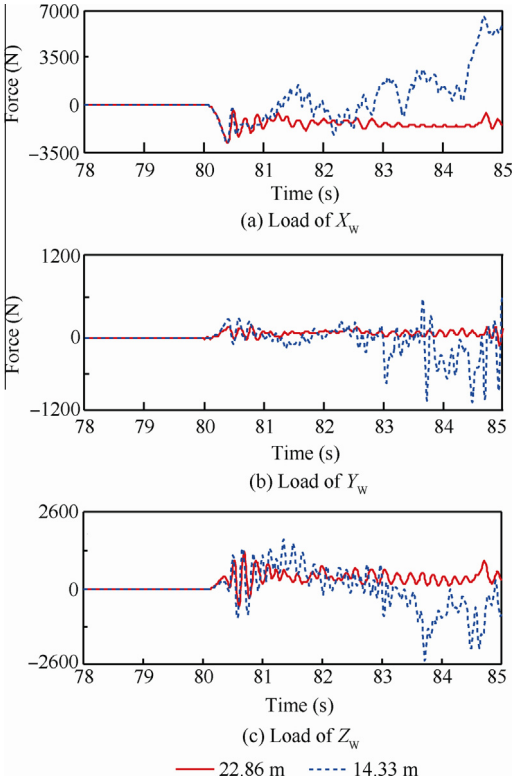

Fig. 11 External forces on probe adopting coupling Profile 1.

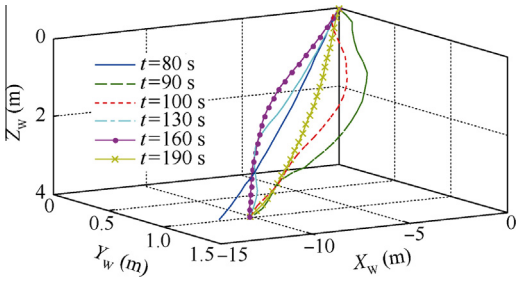

Fig. 12 Hose geometry history controlled by tensator.

Proof The global Lyapunov function is chosen as

$$V = V_2 + \frac{1}{2}s_1^2 + \frac{1}{2}s_2^2 \tag{44}$$

Using Eqs. (29), (34), (38), and (40), as well as differentiating Eq. (44), the derivative of V can be derived as

$$\begin{aligned}\dot{V} &= -k_1 e_1^2 - k_2 e_2^2 - a_1 s_1^2 - a_2 s_2^2 - \rho_1 s_1 \mathrm{sgn}(s_1) - \rho_2 s_2 \mathrm{sgn}(s_2) \\ &= -k_1 e_1^2 - k_2 e_2^2 - a_1 s_1^2 - \rho_1 |s_1| - a_2 s_2^2 - \rho_2 |s_2| \leqslant 0\end{aligned} \tag{45}$$

Eq. (45) is nonpositive definite, namely the global asymptotical stability of the proposed control system is ensured.

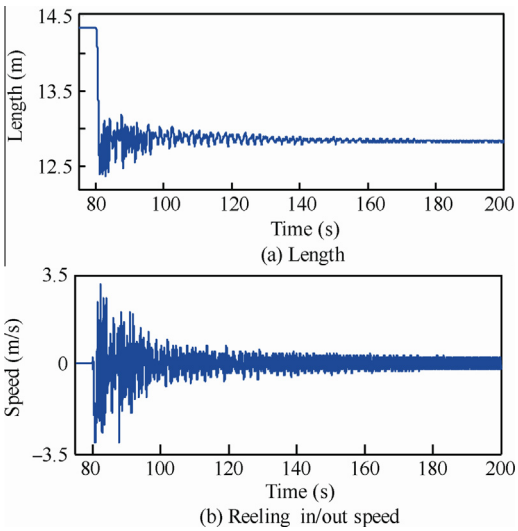

Fig. 13 Length and speed history of hose reeling controlled by tensator.

4. Simulation results

The value of the total number N of the hose model should be determined on the basis of accuracy of modeling, complexity of computation, and length of the hose. N is set equal to 24 here, and other parameters used in simulation are set as follows.

(1) Standard atmosphere plus Dryden wind turbulence is adopted in simulation, and flight altitude and air speed are set equal to 7620 m and 550 km/h, respectively.

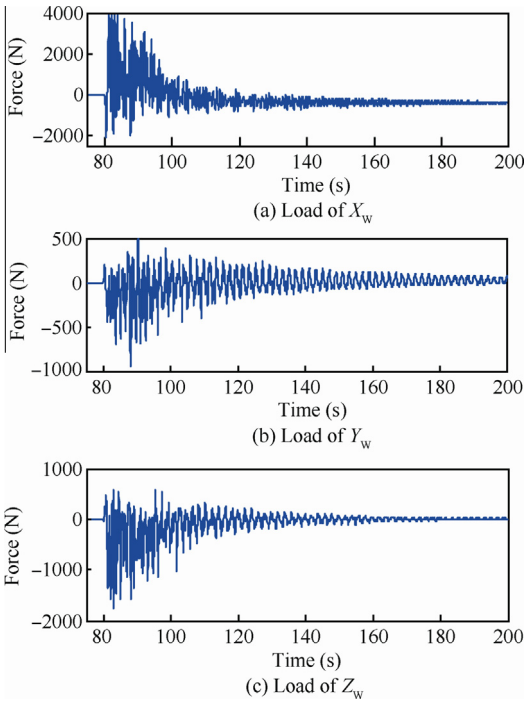

Fig. 15 External forces on probe controlled by tensator.

(2) Parameters of the hose-drogue assembly[11,12]: $\mu = 4.11$ kg/m, $d_k = 0.067$ m, $c_{t,k} = 0.001$, $c_{n,k} = 0.28$, $m_{drogue} = 29.5$ kg, $d_{drogue} = 0.61$ m, and $c_{drogue} = 0.831$.

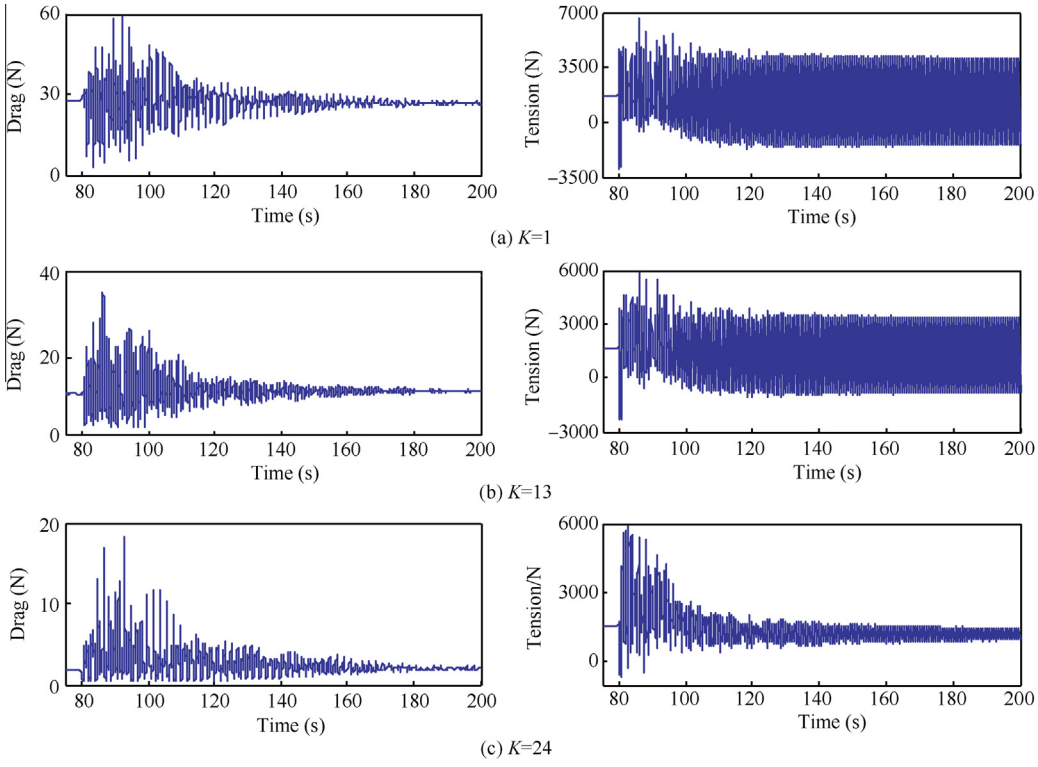

Fig. 14 Drags and tensions of hose controlled by tensator.

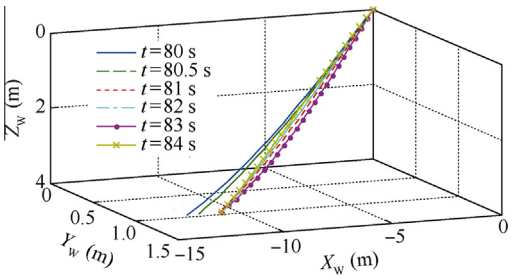

Fig. 16 Hose geometry history controlled by control laws proposed.

(3) Parameters of the PMSM, reducer, and reel:[15] $R = 1.65\,\Omega$, $L_s = 0.0092$ H, $P = 4$, $\psi_f = 0.175$ Wb, $J = 0.001$ kg·m^2, $B = 4.831 \times 10^{-5}$ N·m·s, $i = 10$, $r = 0.06$ m, and $L_1 = 6.5$ m.

(4) Parameters of integral sliding mode backstepping control laws: $k = 1$, $k_1 = k_2 = 50$, $c_1 = c_2 = 0.1$, $a_1 = a_2 = 5$, $\rho_1 = \rho_2 = 8.5$, and $\sigma_i = 0.1$.

With a 39.88 m wing span and a 2.85 m distance between the HDARS and the top of the right wing, the tanker wake is modeled using a Helmholtz horseshoe-vortex model.[21] A vertical slice of the wake 10 m behind the tanker is illustrated in Fig. 2.

4.1. Accuracy of model

Accuracy of the proposed model can be validated directly by steady-state drogue drag and hose tension. Compared with previously reported flight-test data from NASA[6] and research results from Refs.,[11,12] the steady-state drogue drag and maximum hose tension are illustrated in Figs. 3 and 4, respectively.

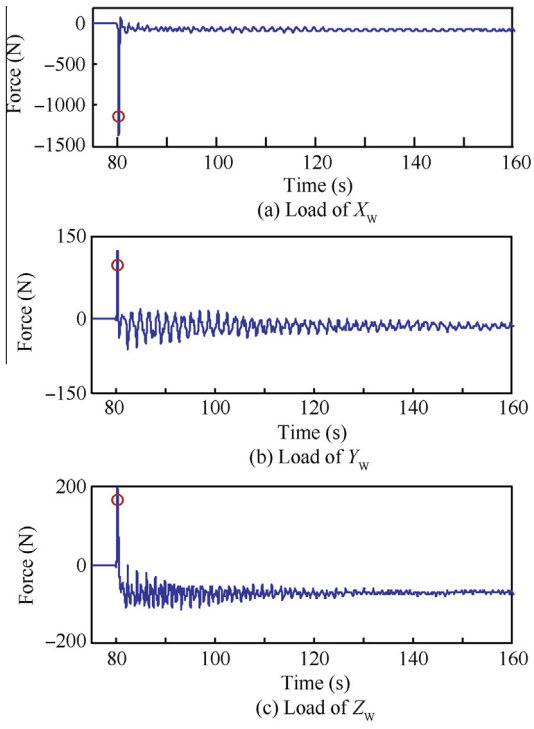

Fig. 18 External forces on probe controlled by control laws proposed.

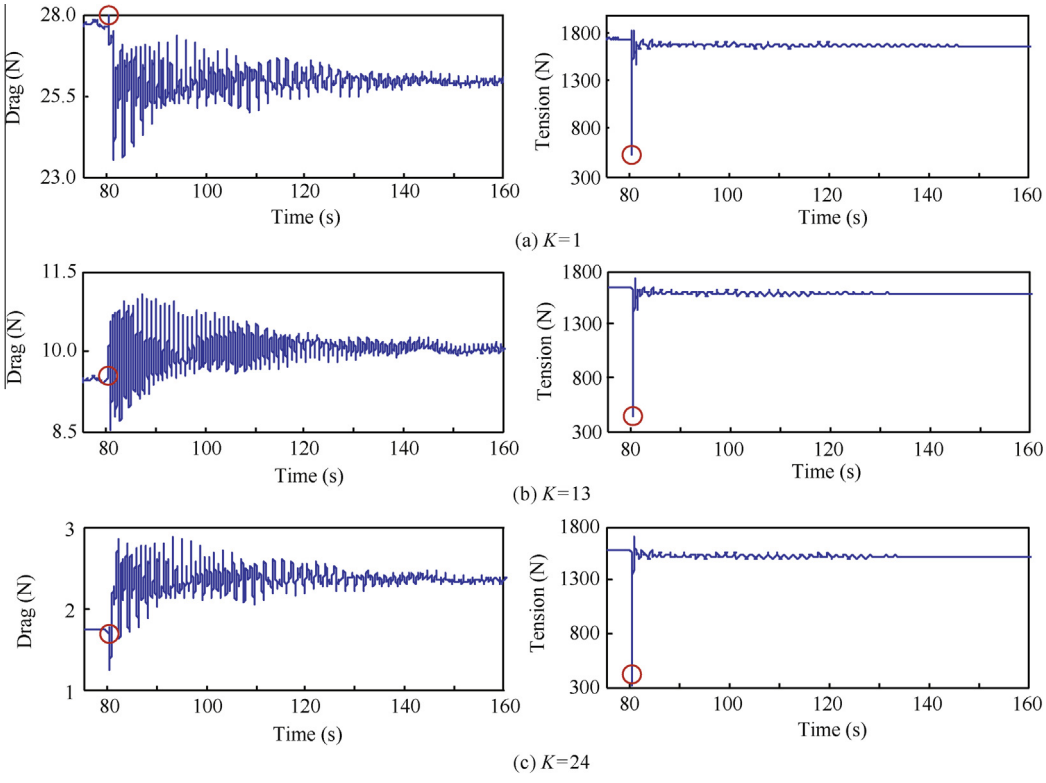

Fig. 17 Drags and tensions of hose controlled by control laws proposed.

As seen in Fig. 3, all the curves of the drogue drag tend to lie below the NASA flight test data,[6] since c_{drogue}, which is selected herein as the same as Ro, et al.[11,12] did, may be a little smaller than its real value. Besides, the difference between the standard atmosphere in modeling and the real atmosphere condition in the NASA flight test[6] may be another reason of the little discrepancy. Figs. 3 and 4 still show good correlations of the model's steady-state characteristics at various altitudes with previously published data from NASA[6] and Refs.[11, 12]

4.2. HWP

To analyze critical influence factors on the HWP, assuming that the reel does not work, the HWP is aroused at various closure speeds and hose lengths by simulation.

4.2.1. HWP at various closure speeds

The hose length is set equal to 22.86 m. Assume that the probe initially contacts the drogue at 80 s, completes hookup with the drogue after 0.25 s, and then pushes the drogue forward along two types of relative coupling profile[4,11] as illustrated in Fig. 5.

Fig. 6 shows the time-history of the hose geometry along two types of relative coupling profile. The HWP is not obvious due to the low degree of the hose slack caused by the shorter distance traveled by the probe along Profile 2, but Profile 1 is exactly opposite of a bond.

Fig. 7 shows the aerodynamic drags and tensions of the 1st, 13th, and 24th segment hose, and Fig. 8 shows the external forces on the probe.

From Figs. 7 and 8, when the aerodynamic drag on the drogue is completely absorbed by the probe during the interval of hookup, there occurs a rapid drop of the hose tension. It is caused by the axial tension's instant transmission property resulted from neglecting the hose's elasticity and damping in modeling. Aerodynamic drags lag behind the tension. As the probe pushes the drogue forward, the hose slack around the drogue increases rapidly. At this moment, the hose starts to whip violently compelled by aerodynamic forces due to the low level of the tension. After that, the whipping goes more violent and travels toward the pod gradually owing to alternate influences of the tension and the drag. As a result, the hose tension around the drogue continues to increase out of control. In the process of the HWP, the tension may vanish, and even turn to be negative as the hose slacks somewhere along the hose, but the singularity problem does not occur at all.

In this process, external forces acting on the probe also increase rapidly with a serious non-axial oscillation. This oscillation generates high loads which can break the hose and the probe, and even causes catastrophic accidents. The HWP will worsen owing to the interference caused by tanker wake and atmospheric turbulence.

4.2.2. HWP at various hose lengths

The hose length is set equal to 14.33 m. Assume that the probe completes coupling as mentioned above along Profile 1 as illustrated in Fig. 5.

During coupling, the time-history of the hose geometry is shown in Fig. 9, the aerodynamic drags and tensions of the 1st, 13th, and 24th segment hose are shown in Fig. 10, and the external forces on the probe are shown in Fig. 11.

Comparing Fig. 6(b), Fig. 9–11, making a uniform coupling along Profile 1, when the hose length is 14.33 m which is much shorter than 22.86 m, the weight of the hose out of the pod is lighter and the hose lies closer to the core of the tanker wake as shown in Fig. 2. Under this condition, the degree of hose slack induced by coupling is much higher, and the HWP goes more violent. The extent of the whipping, the tension at the end of the hose, and the external forces acting on the probe increase sharply out of control in just 5 s. The hose thereby loses stability and quickly turns into a chaotic state of motion.

To sum up, the longer distance the probe moves forward and the shorter the hose length is, the more violent the HWP goes. For this situation, it is significant to develop a quick and efficient HWP suppression strategy for AAR's success rates and security.

It is important to note that the extent of the HWP in simulation may be slightly higher than that in reality due to the neglect of hose's elasticity and damping in modeling.

4.3. PMSM integral sliding mode backstepping position control for HWP

The initial hose length is set equal to 14.33 m and the coupling Profile 1 is chosen, where the HWP is more violent. Assume that the coupling process is set as the same as in Section 4.2.2, and then PMSM integral sliding mode backstepping position control for the HWP is analyzed as follows.

4.3.1. Results of tensator control

When the reel is driven by the tensator, the time-history of the hose geometry is shown in Fig. 12, the length and speed history of the hose motion driven by the reel are shown in Fig. 13, the aerodynamic drags and tensions of the 1st, 13th, and 24th segment hose are shown in Fig. 14, and the external forces on the probe are shown in Fig. 15.

As shown in Figs. 12–15, although the tensator can respond rapidly and retract the hose as the drogue is pushed forward by the probe, the inherent property of simple harmonic vibration is aroused by coupling operation and the wake. This property

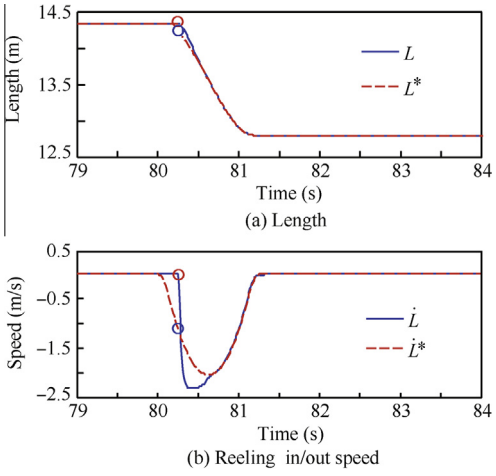

Fig. 19 Length and speed histories of hose reeling controlled by control laws proposed.

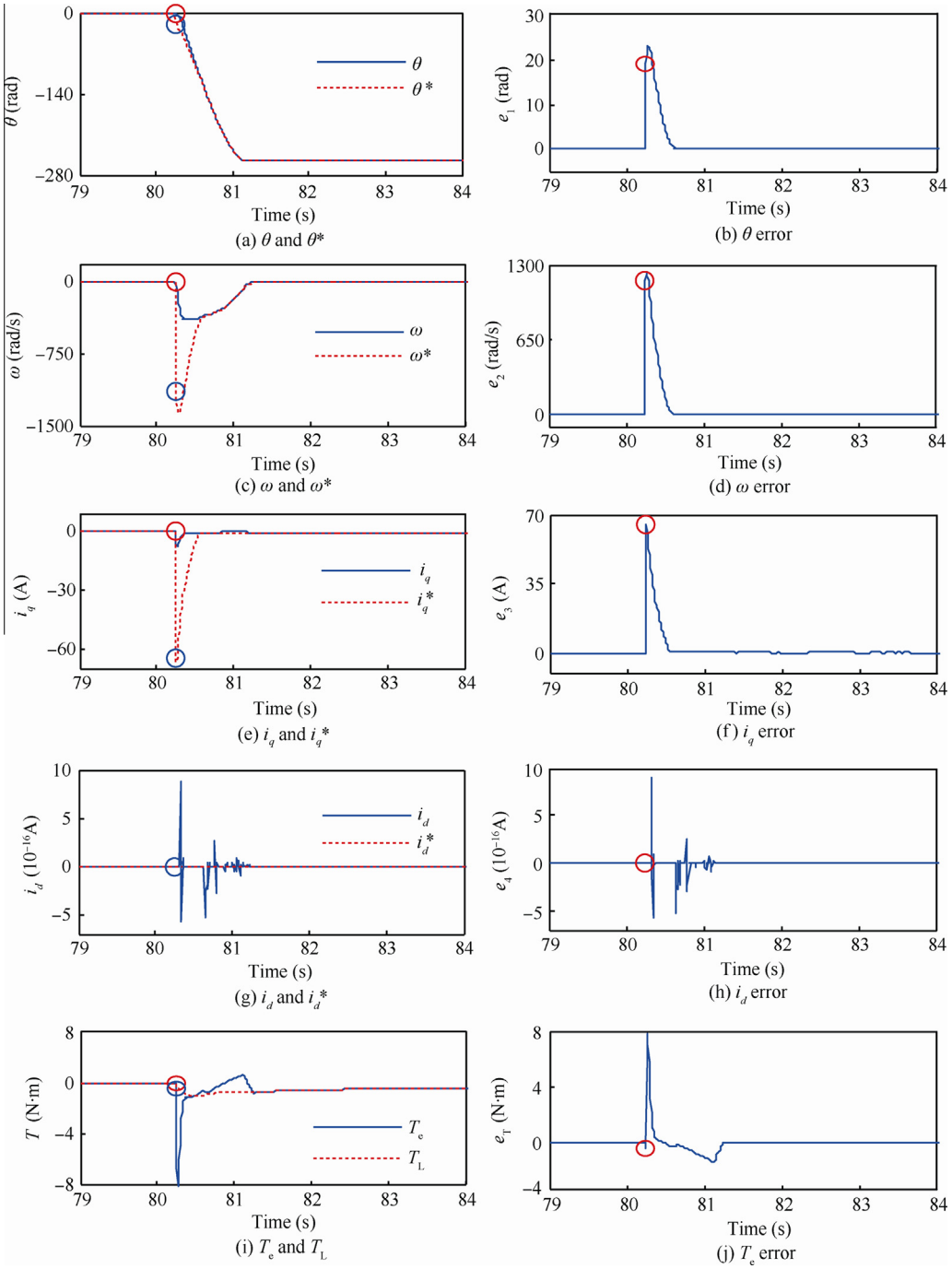

Fig. 20 PMSM state variables of each subsystem controlled by control laws proposed.

compels the hose to whip persistently. As shown in Fig. 12, the hose always whips around the equilibrium position, and the amplitude decreases slowly. As shown in Fig. 13, the length and speed of hose reeling also oscillate persistently. Until $t = 164$ s, the control precision of the hose length goes into a 2% error band. The aerodynamic drags and tensions of the hose also enter a similar state. This violent simple harmonic vibration may cause AAR to fail.

To sum up, interferences caused by excess closure speed by the receiver, tanker wake, and atmospheric turbulence are external reasons why the tensator does not work well for the HWP. In fact, the inherent structure limitation as analyzed above is the root cause.

4.3.2. HWP suppression through PMSM integral sliding mode backstepping position control

Assume that the proposed control laws come to work immediately after completing hookup. Then the time-history of the hose geometry is shown in Fig. 16, the aerodynamic drags and tensions of the 1st, 13th, and 24th segment hose are shown in Fig. 17, the external forces on the probe are shown in Fig. 18, the length and speed histories of the hose reeling

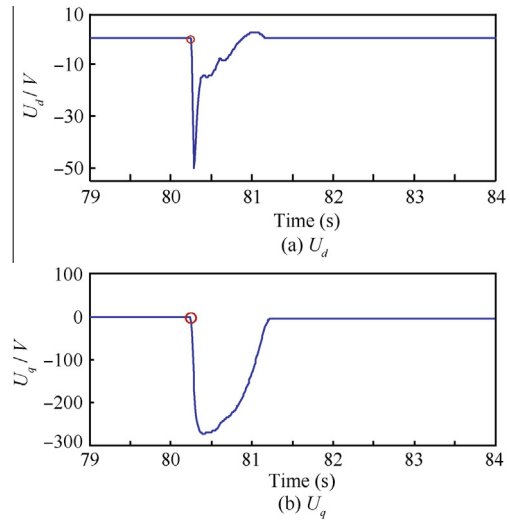

Fig. 21 Real d and q axes voltage inputs controlled by control laws proposed.

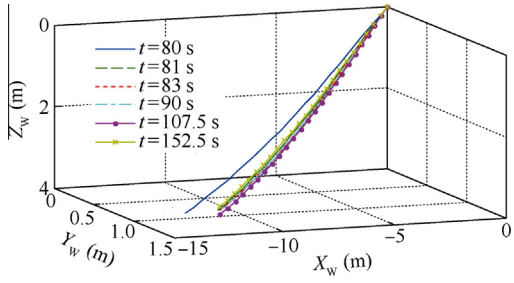

Fig. 22 Hose geometry history with control information deficiency and external disturbance.

driven by the reel are shown in Fig. 19, PMSM state variables of each subsystem are shown in Fig. 20, and the real d and q axis voltage inputs are shown in Fig. 21. The sign (○) denotes the moment when the control laws start to work in the figures.

From Fig. 16, as the probe travels forward, the control laws can retract the hose rapidly and precisely, and keep the catenary shape of the hose steady. The hose slack is maintained at the level just before coupling, and the HWP does not occur at all. Slight hose whipping around the equilibrium position is an unavoidable result of tanker wake and aerodynamic drags.

From Figs. 17 and 18, during the coupling interval from 80 s to 80.25 s, since there exists the hose tension's instant transmission property as mentioned above, a sharp drop of the hose tension and a momentary increase of the axial force on the probe happen after the aerodynamic drags on the drogue is totally absorbed. Then excessive slack of the hose occurs. From Fig. 19, a large initial length and speed tracking error is also generated by the neglect of the hose's elasticity and damping. At t = 80.25 s, the control laws start to retract the hose. At 80.25–81.26 s, the hose is retracted from 14.33 m to 12.79 m. Since the control laws completely match Profile 1, the hose tension recovers rapidly and becomes stable. After that, as the relative distance between the receiver and the tanker does not change any more, the hose length is also maintained to be a constant, and the aerodynamic drags and tensions of the hose gradually become stable as well.

Since a certain extent of the hose slack has arisen from "catch" to "hookup" and the control laws do not work at that time, then as shown in Fig. 20, each subsystem must treat a large initial tracking error. In addition, the load torque T_L is disturbed strongly by the tension's instant transmission property especially under the condition of retracting operation, tanker wake, and atmospheric turbulence. Despite adverse impacts above, the d and q axis currents can track the virtual

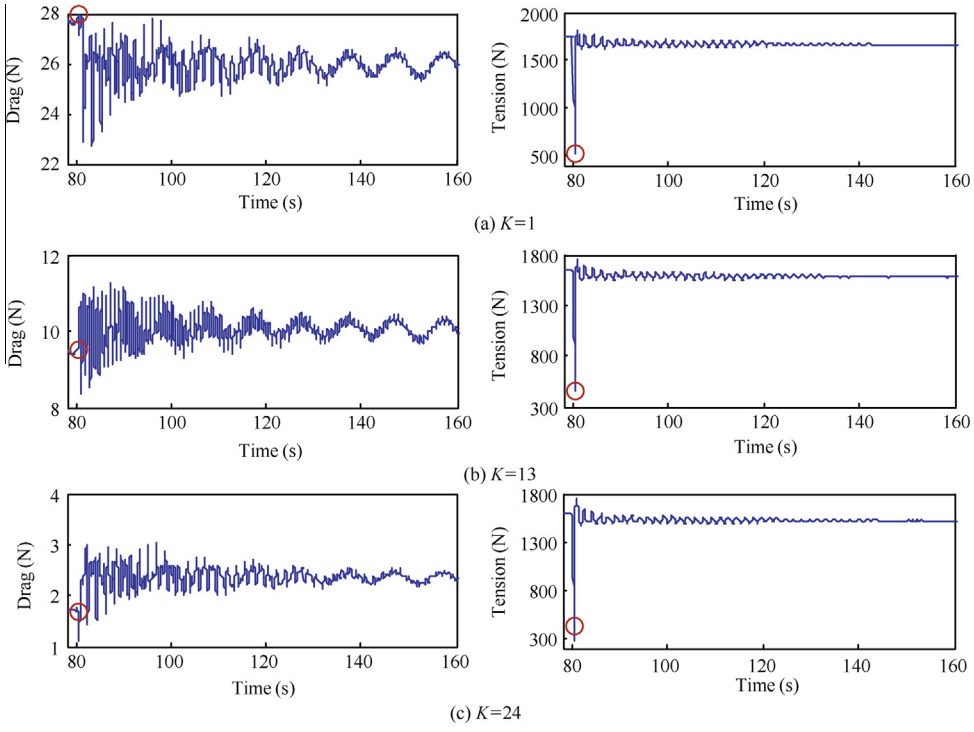

Fig. 23 Drags and tensions of hose with control information deficiency and external disturbance.

commands rapidly and precisely benefitted from responsibility and robustness of the sliding mode surface equations of the d/q axis current error. i_q takes only 0.4 s to overcome the initial tracking error and track the virtual command completely. The d axis current tracking error e_4 is always kept within a 10^{-16} magnitude.

The excellent tracking performance of d and q axis currents leads the PMSM to generate a desired electric torque ensuring the dynamic performance of the whole system. As shown in Fig. 20(i) and (j), at 80.25–81.26 s, as the electric torque T_e drives the PMSM to rotate accurately, the initial tracking errors of ω and θ are overcome and virtual commands can be tracked within only 0.4 s. After that, as the relative distance between the receiver and the tanker does not change any more, the hose is retracted to the desired length, the PMSM does not rotate, the electric torque T_e is completely used to counteract the loads torque, and then all states tend to be stable. The integral factor of the rotor angular tracking error eliminates the static error efficiently, and enhances the performance of hose control.

From Fig. 21, the proposed control laws can ensure the real control inputs stable and bounded. Moreover the chattering phenomenon of sliding mode control is eliminated efficiently.

Comparing the control method through the tensator, PMSM integral sliding mode backstepping position control for the HWP can guarantee the global stability efficiently, and completely match a coupling profile. Consequently, the HWP can be suppressed rapidly and efficiently, and security for AAR can be ensured.

4.4. Robustness analysis

As known from Eqs. (19), (41), and (42), ϑ^*, $\dot{\vartheta}^*$, $\ddot{\vartheta}^*$, and $\dddot{\vartheta}^*$, which include all the information of the coupling profile of the receiver, must be measured indirectly through the relative motion of the receiver. However, a higher-order derivative brings more design difficulty, lower measurement precision, and weaker anti-jamming capability. In addition, the receiver cannot exactly travel along the ideal coupling profile as shown in Fig. 5 in a realistic coupling flight. Its attitude and position could be disturbed by tanker wake and atmospheric turbulence. Then assuming that the higher-order derivatives $\ddot{\vartheta}^*$ and $\dddot{\vartheta}^*$ cannot be obtained in any way, the position of the probe in the vertical direction is disturbed by a sine disturbance such as 0.1 sin ($\pi t/5$) after $t = 90$ s, and other simulation conditions are set as the same as in Section 4.3, the robustness of the control laws is analyzed as follows.

The time-history of the hose geometry is shown in Fig. 22, the aerodynamic drags and tensions of the 1st, 13th, and 24th

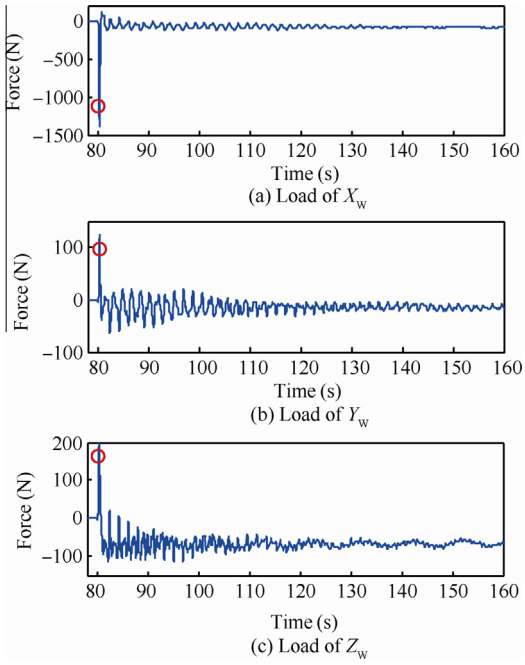

Fig. 24 External forces on the probe with control information deficiency and external disturbance.

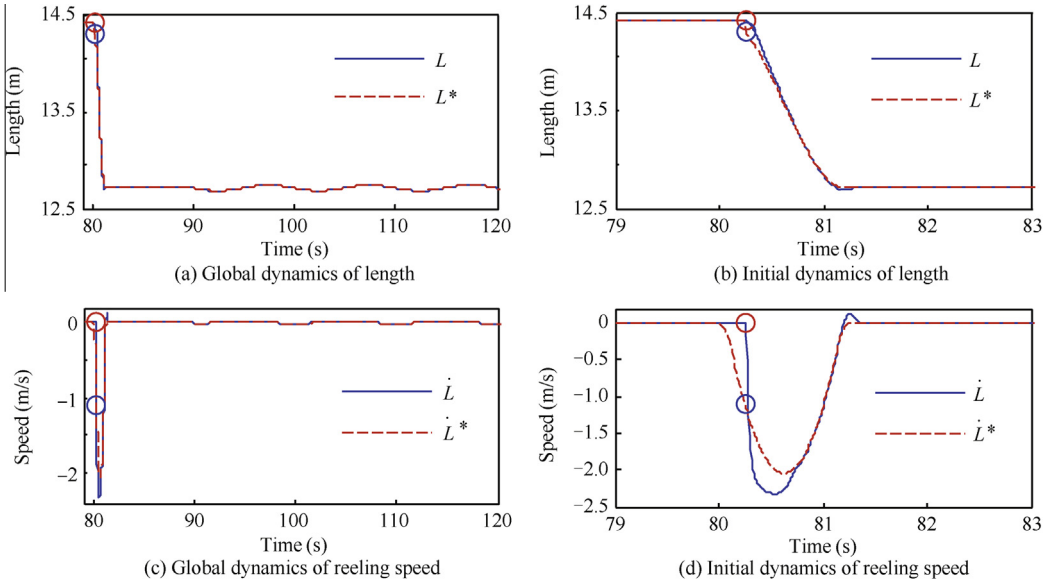

Fig. 25 Length and speed histories of hose reeling with control information deficiency and external disturbance.

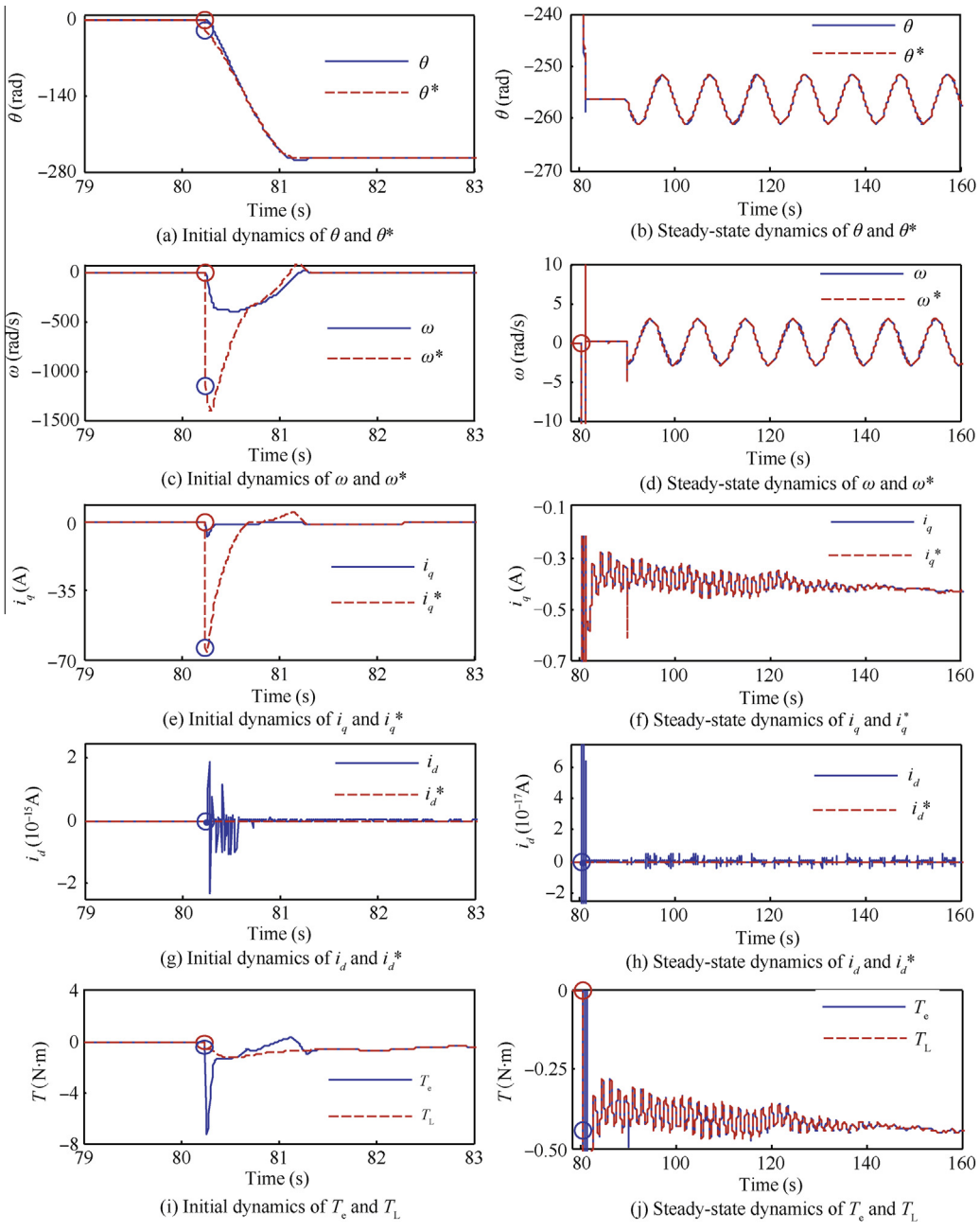

Fig. 26 PMSM state variables of each subsystem with control information deficiency and external disturbance.

segment hose are shown in Fig. 23, the external forces on the probe are shown in Fig. 24, the length and speed histories of the hose reeling driven by the reel are shown in Fig. 25, PMSM state variables of each subsystem are shown in Fig. 26, and the real d and q axis voltage inputs are shown in Fig. 27. The sign "○" has the same meaning as above.

As seen in Fig. 22, at 80–90 s, although $\ddot{\vartheta}^*$ and $\dddot{\vartheta}^*$ cannot be obtained in any way, the control laws can retract the hose rapidly and precisely, and keep the catenary shape of the hose steady as similarly as in Section 4.3.

After $t = 90$ s, the probe, just like a vibration source, compels the drogue to travel up and down around the initial altitude periodically. If without any control, the sine wave will travel toward the pod under the influences of tanker wake and atmospheric turbulence, and the wave-type HWP will occur later. With the compensation provided by the control laws, the catenary shape of the hose can always be kept steady. The sine wave disturbance does not travel along the hose to induce the HWP.

From Figs. 23–25, because $\ddot{\vartheta}^*$ and $\dddot{\vartheta}^*$ cannot be measured, the overshoot of length and speed tracking of the hose reeling increases a little, but responsibility and precision are not impacted. Consequently, even without full control information, the proposed control laws can match the coupling profile to wind or rewind the hose rapidly and precisely. The drags and tensions of the hose as well as the external forces on the probe change into a sine tracking state around the corresponding equilibrium point to compensate the sine wave position

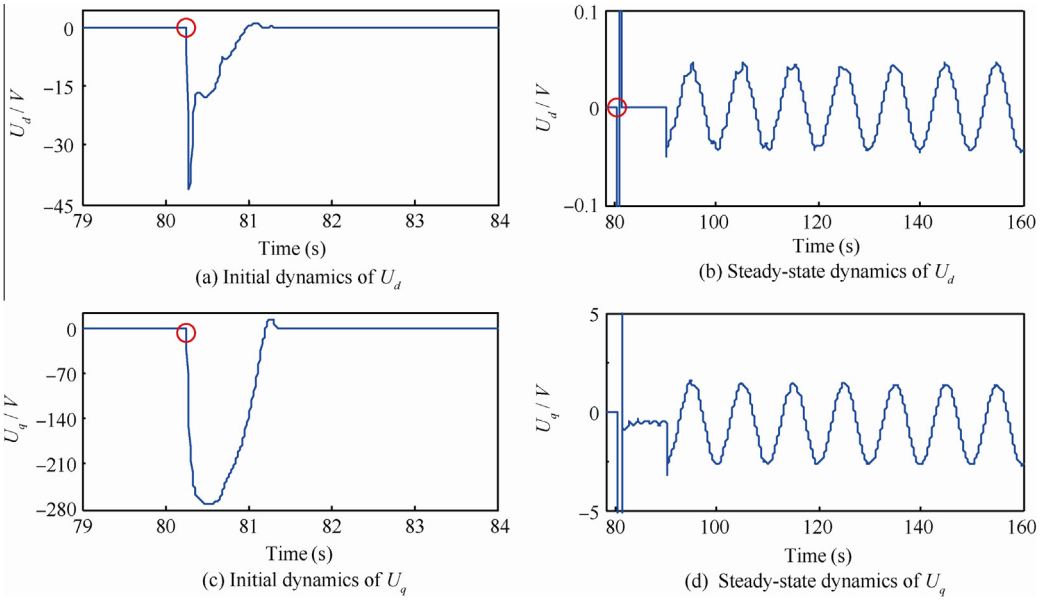

Fig. 27 Real d and q axes voltage inputs with control information deficiency and external disturbance.

disturbance from the probe. Ultimately the HWP is efficiently suppressed by the control laws with the control information loss and the position disturbance.

From Figs. 26 and 27, the overshoot of state variables tracking in each subsystem increases a little without the information about $\ddot{\vartheta}^*$ and $\dddot{\vartheta}^*$, but tracking responsibility and precision are not impacted. The control laws can use the limited command information sufficiently to urge state variables into a dynamic tracking state and compensate the sine wave position disturbance from the probe. With the control information loss and the position disturbance, the proposed control laws can still ensure the real control inputs stable and bounded and eliminate the chattering phenomenon of sliding mode efficiently.

Overall, when there exist control information deficiency and external disturbance, the proposed control strategy can compensate adverse impacts efficiently, guarantee global stability of the whole system, and have a strong robustness to suppress the HWP.

5. Conclusions

(1) The dynamic model of the hose-drogue assembly with a variable length in this paper can reflect dynamics of the hose-drogue assembly and support the exploitation of HWP suppression methods. It can be used as an all-purpose model of variable-length hose-drogue assembly in AAR research.

(2) Relying on a permanent magnet synchronous motor and high-precision position sensors, a new control strategy of suppressing the HWP on the basis of the relative position between the tanker and the receiver is proposed, which overcomes the imperfection of the tensator.

(3) Considering the strict-feedback configuration of the PMSM, a rotor position control law based on the backstepping method is designed with an integral of the rotor position error and an exponential sliding mode reaching law of the current errors. Global stability, accuracy, and robustness can be guaranteed in theory.

(4) The robustness against control information deficiency can greatly relax the requirement on the number of sensors and simplify the control system realization. It is still important to note that measurement precision of relative position and speed sensors installed in the tanker, receiver, and drogue must be ensured to avoid performance degradation.

(5) Compared with the reality, there still exists a certain extent of discrepancy in modeling and controller design to research in future, for example, a momentary compressive load during the interval of hookup caused by the neglect of the hose's elasticity and damping, and the impacts of backlash and friction in the PMSM on the performance of the proposed controller.

Acknowledgement

This study was supported by the National Natural Science Foundation of China (No. 61304120).

References

1. Dong XM, Xu YJ, Chen B. Progress and challenges in automatic aerial refueling. *J Air Force Eng Univ Nat Sci Edn* 2008;**9**(6):1–5 Chinese.
2. Tandale MD, Bowers R, Valasek J. Trajectory tracking controller for vision-based probe and drogue autonomous aerial refueling. *J Guid Control Dyn* 2006;**29**(4):846–57.
3. Ding M, Wei L, Wang BF. Vision-based estimation of relative pose in autonomous aerial refueling. *Chin J Aeronaut* 2011;**24**(6):807–15.
4. Vassberg JC, Yeh DT, Blair AJ, Evert JM. Numerical simulations of KC-10 wing-mount aerial refueling hose-drogue dynamics with a reel take-up system. *21st applied aerodynamics conference*; 2003.

5. Vassberg JC, Yeh DT, Blair AJ, Evert JM. Dynamic characteristics of a KC-10 wing-pod refueling hose by numerical simulation. *20th applied aerodynamics conference*; 2002.
6. Vachon MJ, Ray RJ. Calculated drag of an aerial refueling assembly through airplane performance analysis. *42nd AIAA aerospace sciences meeting and exhibit*; 2004.
7. Hansen JL, Murray JE, Campos NV. The NASA Dryden flight test approach to an aerial refueling system; 2005. Report No.: NASA/TM-2005-212859.
8. Zhu ZH, Meguid SA. Elastodynamic analysis of aerial refueling hose using curved beam element. *AIAA J* 2006;**44**(6):1317–24.
9. Zhu ZH, Meguid SA. Modeling and simulation of aerial refueling by finite element method. *Int J Solids Struct* 2007;**44**:8057–73.
10. Ro K, Basaran E, Kamman JW. Aerodynamic characteristics of paradrogue assembly in an aerial refueling system. *J Aircraft* 2007;**44**(3):963–70.
11. Ro K, Kamman JW. Modeling and simulation of hose-paradrogue aerial refueling systems. *J Guid Control Dyn* 2010;**33**(1):53–63.
12. Ro K, Ahmad H, Kamman JW. Dynamic modeling and simulation of hose-paradrogue assembly for mid-air operations. *AIAA infotech @ aerospace conference*; 2009.
13. Ro K, Kuk T, Kamman JW. Dynamics and control of hose-drogue refueling systems during coupling. *J Guid Control Dyn* 2011;**34**(6):1694–708.
14. Alden RE, Vennero GG, inventor; Whittaker Controls Inc., assignee. Aerial refueling system. United States patent US 5141178. 1992 Aug 25.
15. Liu JK, Sun FC. Nominal model-based sliding mode control with backstepping for 3-axis flight table. *Acta Aeronaut Astronaut Sin* 2006;**19**(1):65–71 [Chinese].
16. Yang Q, Liu WG, Luo GZ. Integral sliding mode backstepping speed control for high-altitude electric propulsion system. *Electr Mach Control* 2012;**16**(6):50–6 [Chinese].
17. Zhang XG, Sun LZ, Zhao K, Sun L. Nonlinear speed control for PMSM system using sliding-mode control and disturbance compensation techniques. *IEEE Trans Power Electron* 2013;**28**(3):1358–65.
18. Bartov A, inventor. Method for engaging a probe and drogue for aerial refueling. United States patent US 6786455B1. 2004 Sep 7.
19. Farrell JA, Polycarpou M, Sharma M, Dong WJ. Command filtered backstepping. *IEEE Trans Automat Control* 2009;**54**(6):1391–5.
20. Zhao Y, Sheng YZ, Liu XD. Sliding mode control based guidance law with impact angle constraint. *Chin J Aeronaut* 2014;**27**(1):145–52.
21. Dogan A, Lewis TA, Blake W. Flight data analysis and simulation of wind effects during aerial refueling. *J Aircraft* 2008;**45**(6):2036–48.

Wang Haitao received his B.S. and M.S. degrees from Air Force Engineering University in 2009 and 2011, respectively. He is now pursing his Ph.D. degree there. His main research interests include system modeling, control and simulation of aerial refueling.

Dong Xinmin is a professor at Air Force Engineering University. He received his B.S. and M.S. degrees from Northwestern Polytechnical University in 1983 and 1988, respectively, and then received his Ph.D. degree from Xi'an Jiaotong University in 1991. He has worked in the field of flight control for more 20 years, and his current research interests include modern control theory, machine vision, and autonomous aerial refueling.

Xue Jianping is an associate professor at Air Force Engineering University. He received his B.S. and M.S. degrees from Air Force Engineering University in 1992 and 2005, respectively. His current research interests include computer control and system simulation.

Liu Jiaolong received his B.S. and M.S. degrees from Air Force Engineering University in 2011 and 2013, respectively. He is now pursing his Ph.D. degree there. His main research interests include CFD analysis and learning control.